$Zn_{13}Sb_{10}$: A Structural and Landau Theoretical Analysis of Its Phase Transitions

Yurij Mozharivskyj,† Yuri Janssen,‡ Joel L. Harringa,‡ Alfred Kracher,‡
Alexandra O. Tsokol,‡ and Gordon J. Miller*,‡,§

Department of Chemistry, McMaster University, Hamilton, Ontario, Canada L8S 4M1, Ames Laboratory, Iowa State University, Ames, Iowa 50011-3020, and Department of Chemistry, Iowa State University, Ames, Iowa 50011-3110

Received July 15, 2005. Revised Manuscript Received December 1, 2005

Composition, crystal structures, polymorphic transformations, and stability of the thermoelectric material known in the literature as "Zn_4Sb_3" have been studied on a polycrystalline sample and Bi-flux-grown single crystals using X-ray diffraction techniques, resistance, and Seebeck coefficient measurements at various temperatures ranging from 4 to 773 K. Microprobe analysis yields the composition of the flux-grown crystals to be close to $Zn_{13}Sb_{10}$, with minor Bi doping. High-temperature X-ray and Seebeck coefficient studies show that the phase is unstable at high temperatures in a vacuum because of Zn losses. Both X-ray diffraction and resistivity measurements indicate the presence of two consecutive symmetry-breaking transitions below room temperature, in agreement with our previous results on polycrystalline samples. Application of Landau theory suggests that the first $R\bar{3}c \rightarrow C2/c$ symmetry breaking may be second-order in nature. The second, low-temperature symmetry breaking may proceed along two routes. One of these pathways, a first-order $C2/c \rightarrow C1$ symmetry reduction, may lead to an incommensurate structure and is consistent with our experimental observations.

Introduction

The recent elucidation of the crystal structure of the state-of-the-art thermoelectric material "Zn_4Sb_3" produces a better understanding of its unique physical properties.[1−3] According to Slack's nomenclature,[4] Zn_4Sb_3 is a real "phonon-glass and electron-crystal". Large atomic deficiencies (~10%) on the main Zn site and presence of additional, partially occupied Zn sites in room-temperature β-Zn_4Sb_3 effectively dampen heat-carrying phonons: the thermal conductivity of Zn_4Sb_3 approaches that of amorphous materials.[5] On the other hand, the electrical conductivity retains values typical for heavily doped semiconductors.[5,6]

The process of establishing the crystal structure of β-Zn_4Sb_3 has been quite remarkable and shows how complementary approaches can yield a coherent picture. The first studies on Zn_4Sb_3 were fueled by the search for new semiconductors and can be traced back to the 1960s and 1970s.[7−10] Zn_4Sb_3 was found to undergo two solid−solid phase transitions: (1) $\alpha \leftrightarrow \beta$ over the 253−263 K temperature range and (2) $\beta \leftrightarrow \gamma$ at ~763 K.[7,8,11] The room-temperature β-structure was initially determined by Bokii and Klevtsova[12] (giving the refined X-ray formula of Zn_6Sb_5) and then by Mayer et al.,[13] who introduced and refined a Zn/Sb mixture on one of the two Sb sites to retain the initial Zn_4Sb_3 sample composition. Further research done by Tapiero et al.[14] showed that Zn_4Sb_3 is zinc deficient ($Zn_{4-\delta}Sb_3$) and revealed its instability at elevated temperatures: annealing of the Zn_4Sb_3 sample in a vacuum at 673 K leads to a significant reduction of the Zn content.

Interest in Zn_4Sb_3 recently revived when a high thermoelectric figure of merit ($ZT = 1.3$ at 670 K) was reported.[5] Attempts to establish the true crystal structure of β-Zn_4Sb_3 ensued. We performed room-temperature X-ray single-crystal analysis and proposed the formula $Zn_{6-\delta}Sb_5$ (we found there is no Zn/Sb mixture and the Zn site is ~90% occupied).[15]

---

* To whom correspondence should be addressed. E-mail: gmiller@iastate.edu.
† McMaster University.
‡ Ames Laboratory, Iowa State University.
§ Department of Chemistry, Iowa State University.

(1) Snyder, G. J.; Christensen, M.; Nishibori, E.; Caillat, T.; Iversen, B. B. *Nat. Mater.* **2004**, *3*, 458−463.
(2) Cargnoni, F.; Nishibori, E.; Rabiller, P.; Bertini, L.; Snyder, G. J.; Christensen, M.; Gatti, C.; Iversen, B. B. *Chem.− Eur. J.* **2004**, *10*, 3861−3870.
(3) Nylen, J.; Andersson, M.; Lidin, S.; Haeussermann, U. *J. Am. Chem. Soc.* **2004**, *126*, 16306−16307.
(4) Slack, G. A. In *CRC Handbook of Thermoelectrics*; Rowe, D. M., Ed.; CRC Press: Boca Raton, FL, 1995; pp 407−440.
(5) Caillat, T.; Fleurial, J. P.; Borshchevsky, A. *J. Phys. Chem. Solids* **1997**, *58*, 1119−1125.
(6) Souma, T.; Nakamoto, G.; Kurisu, M. *J. Alloys Compds.* **2002**, *340*, 275−280.
(7) Shevchenko, V. Y.; Skripkin, V. A.; Ugai, Y. A.; Marshakova, T. A. *Izv. Akad. Nauk SSSR, Neorg. Mater.* **1968**, *4*, 1359−1360.
(8) Ugai, Y. A.; Marshakova, T. A.; Shevchenko, V. Y.; Demina, N. P. *Izv. Akad. Nauk SSSR, Neorg. Mater.* **1969**, *5*, 1381−1385.
(9) Ugai, Y. A.; Marshakova, T. A.; Ignat'ev, N. A.; Aleinikova, K. B. *Tr. Voronezh. Univ.* **1971**, No. 74, 7−10.
(10) Shevchenko, V. Y.; Goncharenko, G. I.; Dvoryankin, V. F.; Ugai, Y. A.; Marshakova, T. A. *Izv. Akad. Nauk SSSR, Neorg. Mater.* **1971**, *7*, 312−313.
(11) Vuillard, G.; Piton, J. P. *C. R. Acad. Sci., Ser. C: Sci. Chim.* **1966**, *263*, 1018−1021.
(12) Bokii, G. B.; Klevtsova, R. F. *Zh. Strukt. Khim.* **1965**, *6*, 866−871.
(13) Mayer, H. W.; Mikhail, I.; Schubert, K. *J. Less-Common Met.* **1978**, *59*, 43−52.
(14) Tapiero, M.; Tarabichi, S.; Gies, J. G.; Noguet, C.; Zielinger, J. P.; Joucla, M.; Loison, J. L.; Robino, M.; Herion, J. *Sol. Energy Mater.* **1985**, *12*, 257−274.
(15) Mozharivskyj, Y.; Pecharsky, A. O.; Bud'ko, S.; Miller, G. J. *Chem. Mater.* **2004**, *16*, 1580−1589.

10.1021/cm0515505 CCC: $33.50

As shown by other studies, this structural information was incomplete: additional, partially occupied Zn sites were not detected by us in β-Zn_4Sb_3. Three extra Zn sites with occupancies of 6.8, 6.8. and 3.3% were discovered using a maximum entropy method (MEM) analysis of synchrotron powder diffraction data.[1,2] The resulting $Zn_{12.82(5)}Sb_{10}$ (or $Zn_{3.85(2)}Sb_3$) composition[2] implies electron deficiencies (the full occupancy of the valence band is expected at $Zn_{13}Sb_{10}$) and, thus, p-type doping of β-Zn_4Sb_3, as found experimentally.[5]

Further insight into the structural features of Zn_4Sb_3 comes from the work by Nylen et al.,[3] who studied the low-temperature α-Zn_4Sb_3 at 150 K. They observed a rhombohedral-to-triclinic symmetry reduction upon cooling, accompanied by complete ordering of the additional interstitial Zn atoms in α-Zn_4Sb_3. No deficiencies were found for either the “main” or the “extra” Zn atoms, thus yielding the $Zn_{13}Sb_{10}$ ($Zn_{3.9}Sb_3$) composition for low-temperature α-Zn_4Sb_3. As pointed out by Nylen et al., it is unlikely that the composition of Zn_4Sb_3 changes during the $\alpha \rightarrow \beta$ transition from $Zn_{13}Sb_{10}$ to $Zn_{12.82}Sb_{10}$. It is possible that slight Zn deficiencies were not detected by Nylen et al. in the low-temperature modification[3] and not all Zn atoms were located by Cargnoni et al. in the room-temperature modification.[2] Slight Zn deficiencies (the $Zn_{13-\delta}Sb_{10}$ formula) could account for the observed p-type conductivity[5] and the temperature dependence of the conductivity,[15] which indicates an extrinsic character of the conductivity resulting from the presence of empty states in the valence band.

Another unresolved issue is the number and nature of the low-temperature phase transitions. Souma et al.[6] studied resistivity and other physical properties of Zn_4Sb_3 at low temperatures and reported only one phase transition, known as the $\alpha \leftrightarrow \beta$ one. In our opinion, the anomalies in the resistivity, as seen in their plots, may have indicated two consecutive transitions. Their experiments also showed that the $\alpha \leftrightarrow \beta$ transition temperature depends strongly on the preparation technique: T_t is 257.4 and 236.5 K, respectively, for samples prepared by gradient-freeze and sintering methods. Our recent studies of heat capacity and resistance on a polycrystalline sample indicated the existence of *two* low-temperature phase transitions: one at 234 K and the other at 254 K.[15] We believe that the triclinic structure at 150 K, reported by Nylen et al.,[3] refers to the low-temperature polymorph α-Zn_4Sb_3 and that the rhombohedral structure, given by Cargnoni et al.,[2] describes the room-temperature polymorph β-Zn_4Sb_3, while the structure of the intermediate polymorph is unknown. Also, the nature of the high-temperature $\beta \leftrightarrow \gamma$ transition at 767 K (T_t is taken from Izard et al.)[16,17] and the structure of the γ-phase remain unresolved. In this paper, we will address the composition of Zn_4Sb_3 as well as the number and nature of its structural transitions by using a combination of X-ray diffraction (XRD) and Landau theory.

Experimental Section

Synthesis. The starting materials were pieces of zinc (99.999 wt %, Alfa Aesar), antimony (99.9999 wt %, Alfa Aesar), and bismuth (99.9995 wt %, Alfa Aesar). We prepared both polycrystalline and single-crystal samples. Details on the preparation of the polycrystalline sample with the initial composition of Zn_4Sb_3 can be found in ref 15. Single crystals were grown from a ternary melt, with Bi acting as a flux.[18] The starting elements were combined in the molar ratio 20:10:70 Zn/Sb/Bi in an alumina crucible and sealed in a silica-glass ampule with a partial pressure of argon. The ampule was heated to 650 °C and then slowly cooled, over a period of 60 h, to 290 °C, at which point the remaining melt was decanted. Crystals grown in this way formed blocks with a typical diameter of 1−2 mm.

Microprobe Analysis. Quantitative electron probe microanalysis was performed on a JEOL JXA-8200 Superprobe with 20 kV acceleration potential and 20 nA beam current. Small crystals extracted from the polycrystalline Zn_4Sb_3 sample were not suitable for mounting and polishing; instead, millimeter-size, flux-grown crystals were chosen for the electron probe microanalysis. Pure elements were used as standards. The X-ray lines used for analysis were Zn Kα, Sb Lα, and Bi Mα_1. Counting times of 10 s on the peak and 5 s each for high and low background were used.

Because the fourth-order Zn Kβ line is close to Bi Mα and the third-order Bi Lα_1 line is close to Sb Lα, the pure element standards were also analyzed as unknowns. No interference was detected above the 0.04 wt % level, which is the nominal limit of detection.

Analysis of 33 points indicated only slight Bi doping of the structure and yielded the average composition of $Zn_{56.5(1)}Sb_{43.2(2)}Bi_{0.35(2)}$. Assuming presence of Bi atoms only on the Sb sites (a Sb/Bi substitution), the composition of a Bi-free crystal can be written as $Zn_{56.5}Sb_{43.5}$, which is very close to $Zn_{13}Sb_{10}$ ($Zn_{56.52}Sb_{43.48}$). Thus, the real composition of Zn_4Sb_3 is better represented with the $Zn_{13}Sb_{10}$ formula, as proposed by Nylen et al.[3]

Resistance Measurements. Our previous studies on the polycrystalline sample showed that resistance measurements could serve as a sensitive probe for the number and nature of phase transitions in Zn_4Sb_3.[15] Therefore, we employed the same technique for studying transformational behavior of crystals grown from the Bi flux. Resistance was measured in the 4−350 K range using the standard four-probe method in commercial (Quantum Design) laboratory equipment on a bar cut from one of the crystals (dimensions 0.6 × 0.3 × 2 mm). Contacts to the sample were made with Epotek H20E silver epoxy and Pt wires. Heating and cooling were done at rates of less than 0.5 K/min, and resistance values were recorded every 0.5 K. To explore the nature of the transformations the crystal was cycled through the transition temperatures. Resistivity of the flux-grown single crystal is presented in Figure 1a (only data for the first cycle are plotted). For comparison, resistance for a polycrystalline sample from ref 15 is shown in Figure 1b. Both samples show an increase in resistance with temperature, which is characteristic of both metallic phases and heavily doped (extrinsic) semiconductors.

A generalized look at the resistivity/resistance versus temperature (R vs T) plots for both the single and the polycrystalline samples gives an impression of only *one* λ-shaped transition, but a closer analysis, outlined below, and crystallographic data, given later, clearly indicate *two* separate transitions. As for the polycrystalline sample, the high-temperature transition for the single crystal at 244 K ($T_t = 254$ K for the polycrystalline sample) exhibits no observed hysteresis and may be second-order (continuous) in nature. The newly formed phase is stable in a rather narrow temperature interval

---

(16) Izard, V.; Record, M. C.; Tedenac, J. C. *J. Alloys Compd.* **2002**, *345*, 257−264.

(17) Izard, V.; Record, M. C.; Tedenac, J. C.; Fries, S. G. *CALPHAD: Comput. Coupling Phase Diagrams Thermochem.* **2002**, *25*, 567−581.

(18) Canfield, P. C.; Fisk, Z. *Philos. Mag. B* **1992**, *65*, 1117−1123.

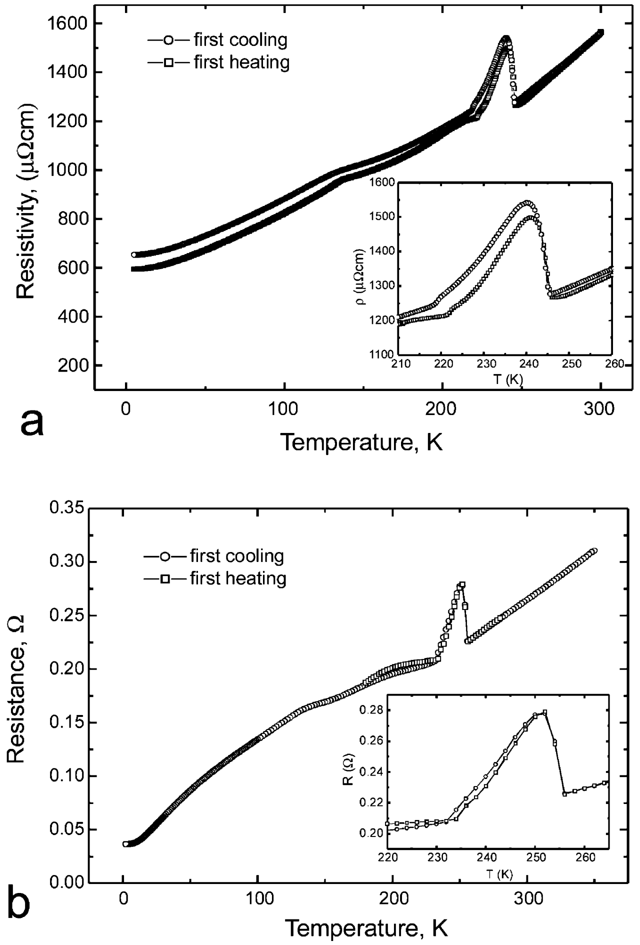

Figure 1. (a) Resistivity of the single-crystal grown from Bi flux and (b) resistance of the Zn_4Sb_3 polycrystalline sample as a function of temperature. The insets show the transition regions.

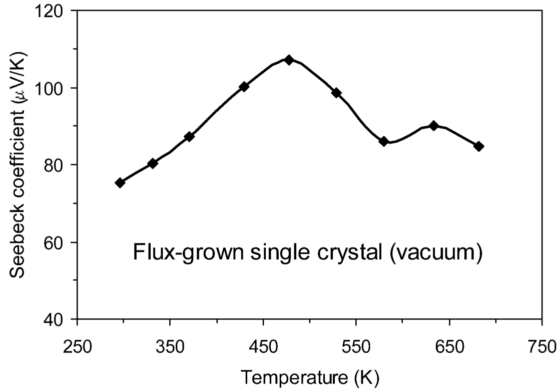

Figure 2. Seebeck coefficient as a function of temperature for the flux-grown single crystal during heating in a vacuum.

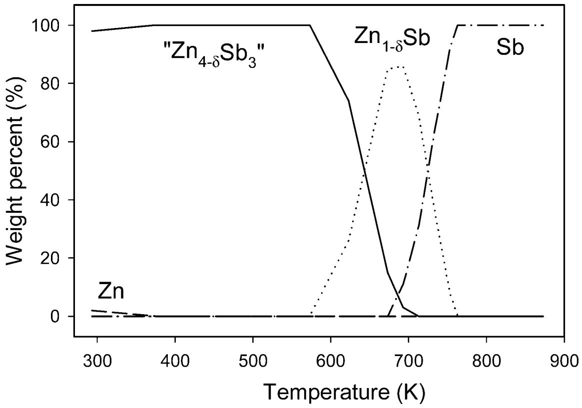

Figure 3. Weight percent of the identified phases in the Zn_4Sb_3 polycrystalline sample during heating (powder XRD data, ref 15).

between 244 and 218 K (254 and 234 K for the polycrystalline sample), below which it transforms into another polymorph, known as an α-form. The second transition bears two features of a first-order phase transition: (1) the presence of hysteresis upon heating and cooling and (2) a sudden change in the slope of R versus T. For the flux-grown crystal, the change in slope of ρ versus T for the low-temperature transition is not as sharp as for the polycrystalline Zn_4Sb_3 sample, because of a steplike feature around the transition temperature, which is present during both heating and cooling. The nature of this feature is not clear at the moment, although it may indicate an additional structural perturbation.

The residual resistance ratio, ρ(300 K)/ρ(5 K) ~ 2.6, for the flux-grown crystal is much lower than that for the polycrystalline sample (~11), which is probably due to the slight Bi doping in the flux-grown crystal and the possible presence of Zn on the grain boundaries of the polycrystalline sample. The transition temperatures are noticeably lower for the single crystal, which most likely results from a small amount of Bi doping, in support of an earlier observation that the transition temperature is dependent on the preparation method. Cycling through the transformation region increases the resistivity of the crystal, which can be associated with the formation of microcracks in the crystal as it is heated and cooled through its crystallographic phase transitions.

Seebeck Coefficient Measurements. A flux-grown single crystal was cut to obtain two parallel opposite faces with a distance of 2.5 mm between them. The Seebeck coefficient was determined by placing the crystal between two spring-loaded Ta wound BN heaters. A Mo core in each heater transferred heat to each end of the crystal. The heaters served both to heat the sample to the target temperature and to generate a temperature gradient across the sample. A 0.35 mm Mo plate was positioned between the crystal end and the Mo heater core. Pt−Pt13%Rh thermocouples were welded to each plate to form an extrinsic thermocouple. The Pt leg of each thermocouple serves as a voltage lead to measure the voltage difference ΔV generated across the sample as the thermal gradient ΔT is imposed. A linear least-squares fit is then applied to the measured $\Delta V/\Delta T$ to obtain the Seebeck coefficient. The average temperature between the top and bottom thermocouples is the reported measurement temperature. The sample was measured from 300 to 673 K under vacuum, and the results are shown in Figure 2.

The room-temperature Seebeck coefficient of 75 μV/K for the flux-grown single crystal is lower than the value of 113 μV/K reported by Caillat et al. for hot-pressed samples.[5] This value is also lower than ~135 μV/K for the sample prepared by the gradient-freeze method but comparable to ~70 μV/K for the sintered polycrystalline sample as reported by Souma et al.[6] (the Seebeck coefficient values are taken from the plot). This comparison clearly indicates that the Seebeck coefficient is strongly dependent on the preparation technique.

The temperature dependence of the Seebeck coefficient (Figure 2) reveals instability of the crystal during heating in a vacuum. On the basis of the high-temperature XRD powder data (Figure 3), the decrease in thermopower above 500 K can be associated with Zn sublimation and development of the zinc-poorer, ZnSb, phase ($Zn_{13}Sb_{10}(s) \rightarrow 10ZnSb(s) + 3Zn(g)$). Subsequent increase in thermopower after 600 K can be linked to further Zn losses and appearance of elemental antimony ($ZnSb(s) \rightarrow Sb(s) + Zn(g)$).

X-ray Analysis. *Room-Temperature, Single-Crystal XRD.* The diffraction data for two single crystals, one extracted from the polycrystalline Zn_4Sb_3 sample and the other Bi-flux-grown, were

Table 1. Crystal Data and Structure Refinements of the Single Crystal from the Polycrystalline Sample at 293 K[a]

	full Zn occupancy	deficient Zn	deficient Zn + extra Zn
composition	$Zn_{12}Sb_{10}$	$Zn_{10.75(5)}Sb_{10}$ $(Zn_{3.23(1)}Sb_3)$	$Zn_{11.8(2)}Sb_{10}$ $(Zn_{3.54(6)}Sb_3)$
data/parameters	438/19	438/20	438/35
goodness of fit on F^2	1.185	1.094	1.122
R indices $[I/\sigma(I) > 2]$	$R_1 = 0.0343$, $wR_2 = 0.0945$	$R_1 = 0.0296$, $wR_2 = 0.0751$	$R_1 = 0.0228$, $wR_2 = 0.0543$
R indices (all data)	$R_1 = 0.0355$, $wR_2 = 0.0952$	$R_1 = 0.0307$, $wR_2 = 0.0758$	$R_1 = 0.0238$, $wR_2 = 0.0547$
extinction coefficient	0.000 29(7)	0.000 27(5)	0.000 36(5)
Peak/hole, e/Å^3	2.517/−1.492	2.296 / −0.998	1.286 and −0.897
Zn occupancy	Zn = 1.00	Zn = 0.896(4)	Zn = 0.907(5) Zn1 = 0.025(4) Zn2 = 0.032(6) Zn3 = 0.022(5)

[a] SMART Apex diffractometer, space group $R\bar{3}c$, $Z = 3$, $a = 12.2200(3)$ Å, $c = 12.4177(5)$ Å, 2θ range = 6.66−56.56°, data completeness to $2\theta_{max}$ is 96.3%.

Table 2. Crystal Data and Structure Refinements of the Single Crystal from the Polycrystalline Sample at 238 K

composition	$Zn_{12.0(2)}Sb_{10}$
space group	*C*2/*c*
lattice parameters, Å	$a = 10.878(2)$ $b = 12.225(2)$, $\beta = 100.044(2)°$ $c = 8.185(1)$
volume, Å^3	1071.8(3)
Z	2
diffractometer	SMART 1000
2θ range	5.06−56.64°
index ranges	$-13 \le h \le 14$, $-16 \le k \le 16$, $-10 \le l \le 10$
independent reflections	1343 ($R_{int} = 0.0330$)
completeness to $2\theta_{max}$	95.7%
data/parameters	1343/70
goodness of fit on F^2	1.055
final *R* indices $[I/\sigma(I) > 2]$	$R_1 = 0.0260$, $wR_2 = 0.0621$
R indices (all data)	$R_1 = 0.0334$, $wR_2 = 0.0662$
extinction coefficient	0.00076(7)
largest diff. peak/hole, e/Å^3	1.360/−1.113

Table 3. Atomic and Equivalent Isotropic Displacement Parameters[a] for the Single Crystal from the Zn_4Sb_3 Polycrystalline Sample

atom		occup.	*x*/*a*	*y*/*b*	*z*/*c*	U_{eq}, Å^2
			$R\bar{3}c$, 293 K			
Zn	36f	0.907(5)	0.24413(8)	0.07926(8)	0.09657(7)	0.0265(3)
Zn1	36f	0.025(4)	0.074(3)	0.250(3)	0.095(2)	0.02(1)
Zn2	36f	0.032(6)	0.202(3)	0.094(3)	0.025(2)	0.04(1)
Zn3	36f	0.022(5)	0.236(3)	0.130(4)	0.234(3)	0.03(1)
Sb1	18e	1	0.35588(4)	0	1/4	0.0167(2)
Sb2	12c	1	0	0	0.1364(1)	0.0162(2)
			C/2*c*, 238 K			
Zn1	8f	0.841(9)	0.0726(3)	0.0890(3)	0.0703(3)	0.020(1)
Zn2	8f	0.932(9)	0.2262(3)	0.2938(3)	0.3419(3)	0.025(1)
Zn3	8f	0.947(9)	0.3878(3)	0.0458(2)	0.01623(3)	0.023(1)
Zn4	8f	0.109(5)	0.313(2)	0.040(1)	0.173(2)	0.035(4)
Zn5	8f	0.102(7)	0.168(2)	0.253(1)	0.219(2)	0.035(5)
Zn6	8f	0.079(6)	0.030(2)	0.066(2)	0.619(3)	0.035(5)
Sb1	8f	1	0.1786(1)	0.0720(1)	0.3942(1)	0.0136(3)
Sb2	8f	1	0.3860(1)	0.2506(1)	0.1373(1)	0.0136(2)
Sb3	4e	1	0	0.3948(2)	1/4	0.0142(5)

[a] Anisotropic temperature factors and other crystallographic details can be obtained in Supporting Information.

collected on a Bruker Apex CCD diffractometer in a full reciprocal sphere with 0.3° scans in ω, with an exposure time of 10−15 s per frame and with $2\theta_{max} = 70°$. Intensities were extracted and then corrected for Lorentz and polarization effects through the SAINT program.[19] Empirical absorption corrections were based on modeling a transmission surface by spherical harmonics employing equivalent reflections with $I > 3\sigma(I)$ (program SADABS).[19]

Structures of both crystals were solved and refined in the $R\bar{3}c$ space group. Because of Zn deficiencies and a small amount of Bi doping, the Bi concentration in the flux-grown crystal could not be reliably refined. The atomic coordinates and occupancies of the flux-grown crystal are analogous within three standard deviations to those of the crystal extracted from the polycrystalline sample. The quality of the flux-grown crystal appears to be lower than that of the crystal extracted from the polycrystalline sample as judged by the R_1 residual values (0.0461 vs 0.0260). Therefore, only data for the latter are discussed hereafter. In agreement with earlier results,[15] significant deficiencies (∼10%) were found for the "main" Zn atoms, site 36f. A difference Fourier map revealed pockets of small electron density around the main Zn site, among which three peaks stood out as possible Zn positions. In line with the single-crystal and MEM powder structural data,[1,2] three interstitial Zn sites were introduced into the structure. The refined coordinates of the additional Zn sites are similar to those reported by Snyder et al.[1] Improvements in the residual values and electron density difference map are outlined in Table 1. The Hamilton test[20] indicated that every consecutive structural model (deficient Zn site and then three extra Zn sites) can be accepted with larger than 0.995 probability. The refinement of the additional Zn positions was done isotropically (anisotropic refinement produced physically unreasonable thermal ellipsoids), and the final crystallographic and atomic parameters standardized through the program TIDY[21] are summarized in Tables 1 and 3. While introducing extra Zn atoms into the structure raised the Zn concentration (Table 1), the refined room-temperature composition $Zn_{11.8(2)}Sb_{10}$ still differs much from the room-temperature $Zn_{12.82(5)}Sb_{10}$ and low-temperature $Zn_{13}Sb_{10}$ compositions reported by Snyder et al.[1] or by Nylen et al.[3], respectively. A lower Zn concentration in $Zn_{11.8(2)}Sb_{10}$ may be due to both intrinsic factors (lower Zn concentration in the crystal, distribution of Zn atoms on more than three additional sites) and extrinsic factors (absorption correction, extinction), which are difficult to account for during the refinement.

Low-Temperature, X-ray Powder Diffraction. To check the number of the symmetry-breaking transitions, we performed low-temperature X-ray powder diffraction. The low-temperature data on the properly ground polycrystalline Zn_4Sb_3 sample were collected on a Rigaku TTRAX rotating anode diffractometer (Mo Kα radiation, $9 \le 2\theta \le 40°$, 0.01° step, 1 s/step scanning time, 10^{-7} Torr dynamic vacuum, ±2 K temperature stability, 70−293 K temperature range). The powder diffraction patterns were recorded every 5 K in the 220−255 K range to embrace the phase transition region. In the absence of structural transitions, better-defined diffraction peaks are obtained upon cooling. However, the opposite effect was observed during our experiment (Figure 4), which is indicative of a symmetry reduction. Because peaks were only broadened but not split, refinement of the lattice parameters in a symmetry setting lower than the hexagonal one always resulted in convergence of the *a* and *b* parameters. Therefore, the lattice parameters were refined in the hexagonal representation (the $R\bar{3}c$ space group), and their temperature dependence is plotted in Figure 5. Nonlinear changes in the unit cell dimensions in the 225−255 K temperature range indicate structural perturbations.

To get a better understanding of these changes, we performed an analysis of peak profiles as a function of temperature. At room

---

(19) *SAINT;* Bruker Analytical X-ray Systems: Madison, WI, 2002.
(20) Hamilton, W. C. *Acta Crystallogr.* **1965**, *18*, 502−510.
(21) Gelato, L. M.; Parthe, E. *J. Appl. Crystallogr.* **1987**, *20*, 139−143.

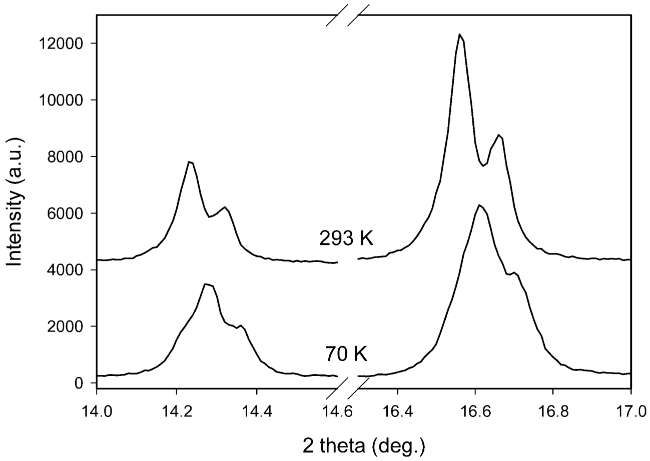

Figure 4. Peak profiles of the Zn_4Sb_3 polycrystalline sample from the powder diffraction at 293 and 70 K. Peak broadening at 70 K indicates symmetry breaking.

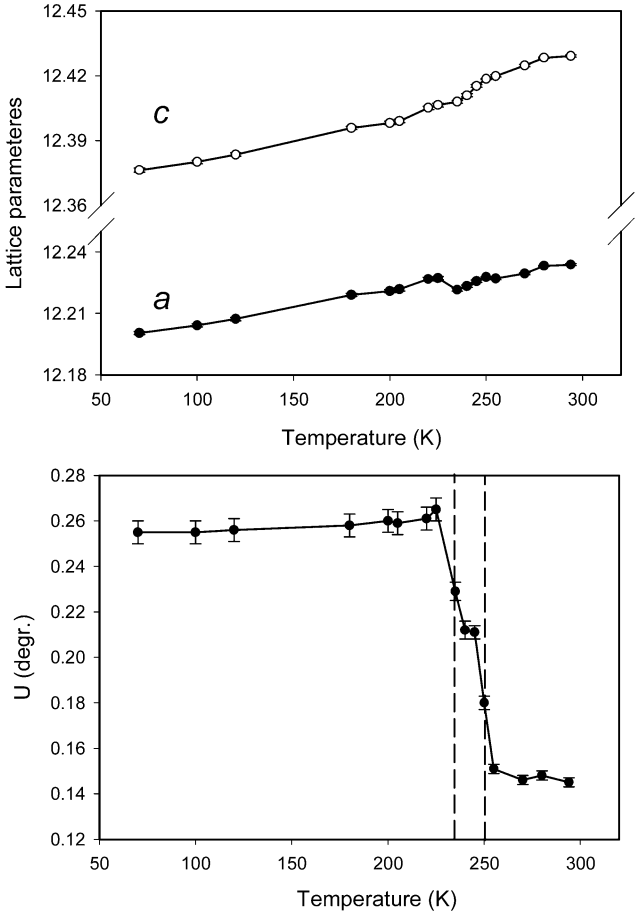

Figure 5. Powder lattice constants and a U parameter describing the peak full width at half-maximum for the Zn_4Sb_3 polycrystalline sample during cooling.

temperature, three parameters, U, V, and W, describing the peak full width at half-maximum ($H = [U \tan^2 \theta + V \tan \theta + W]^{1/2}$) as a function of the angle θ were refined. The variables V and W were then fixed, and only the U parameter was refined at lower temperatures. (In general, the V parameter is negative, U and W are positive, and $U \gg W$. Thus, the biggest positive contribution and the principal angle-dependent broadening of the peaks are associated with the U parameter.) As seen from Figure 5, the value of U nearly doubles upon cooling from 294 to 220 K, which is indicative of symmetry reduction, and then, as expected, it decreases with temperature. A plateau in U at 245 and 240 K separates two sharp increases in the peak width at 250 and 235 K, which can be associated with two consecutive phase transitions observed from the physical property measurements. While it is difficult to evaluate exact transition temperatures because of small temperature resolution and stability during the X-ray powder studies, the transition temperatures of ~250 and ~235 K match well the values obtained by other techniques.

Low-Temperature, Single-Crystal XRD. The low-temperature data for the crystal extracted from the polycrystalline Zn_4Sb_3 sample were taken on a Bruker SMART 1000 CCD diffractometer at 243(1), 238(1), 233(1), 228(1), and 203(1) K. Diffraction data were collected and processed the same way as the room-temperature ones. Indexing of the reflections at 243 and 238 K, below the first β-to-intermediate phase transition temperature, in the rhombohedral setting with unconstrained lattice parameters and angles (i.e., a triclinic approximation) did not indicate significant deviation of the lattice parameters and angles from the rhombohedral ones ($a = b = c$ and $\alpha = \beta = \gamma$): for example, $a = 8.189(1)$ Å, $b = 8.190(1)$ Å, $c = 8.191(1)$ Å, $\alpha = 96.641(2)°$, $\beta = 96.681(2)°$, and $\gamma = 96.649(2)°$ from 989 reflections at 238 K. However, according to the physical property measurements there is a significant structural perturbation on cooling to 238 K. In addition, the low-temperature powder diffraction indicates symmetry reduction in this temperature region. The *translationengleiche*, lower-symmetry subgroups of the $R\bar{3}c$ space group are the monoclinic space groups $R12/c$ ($C2/c$), $R12$ ($C2$), and $R11/c$ (Cc) and the triclinic space groups $R1\bar{1}$ ($C\bar{1}$ or $P\bar{1}$) and $R11$ ($C1$ or $P1$). Because the symmetry reduction proceeds further upon cooling (it is a two-step process according to Figure 5; the resistance measurements (Figure 1) also indicate two consecutive phase transitions), the lattice symmetry at 238 K is likely to be monoclinic and the symmetry at lower temperatures is likely to be triclinic. Analysis of the extinction conditions at 238 K indicated presence of a c glide plane and thus supported formation of the monoclinic lattice upon the first phase transition. Among the two monoclinic space groups $C2/c$ and Cc, $C2/c$ was chosen as the correct one because it led to a stable structural refinement with fewer refined parameters and a smaller number of correlation factors. Besides, the $R\bar{3}c \rightarrow C2/c$ symmetry reduction satisfies the Landau conditions for a second-order phase transition (see below) and, thus, can account for the absence of the hysteresis during the first low-temperature phase transition. Also, only a further symmetry reduction of the $C2/c$ space group and not of the Cc one can yield the $C\bar{1}$ space group, as reported by Nylen et al.[3]

The $R\bar{3}c \rightarrow C2/c$ symmetry breaking can proceed along three equivalent pathways (due to the equivalence of the twofold axis and the c glide planes as discussed below), and because the monoclinic distortion of the rhombohedral cell is very small, the resulting twinning is merohedral according to the single-crystal XRD techniques used. Because of the merohedral nature of twinning, the monoclinic lattice parameters obtained from the least-squares refinement will resemble those derived using the rhombohedral unit cell. The following axial transformation between the rhombohedral and monoclinic settings was used to generate a reference C-centered monoclinic cell with $a = 10.888(2)$ Å, $b = 12.237(2)$ Å, $c = 8.190(1)$ Å, and $\beta = 100.025(2)°$:

$$\begin{pmatrix} a_m \\ b_m \\ c_m \end{pmatrix} = \begin{pmatrix} 1 & 0 & 1 \\ 1 & 0 & -1 \\ 0 & 1 & 0 \end{pmatrix} \begin{pmatrix} a_r \\ b_r \\ c_r \end{pmatrix}$$

During structural refinement the crystal was treated as a twin with three components. This refinement produced a smoother difference electron density map, on which only three sites stood out as possible Zn positions. The refinement with three additional,

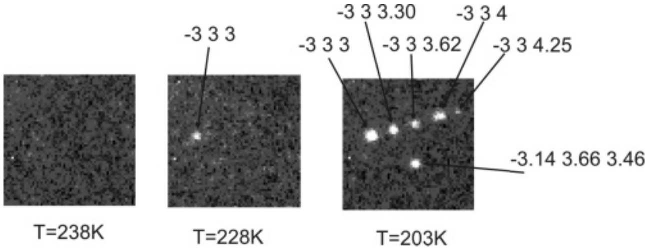

Figure 6. Development of the incommensurate modulation as the crystal is cooled below the second transition temperature.

partially occupied Zn sites yielded a $Zn_{12.0(2)}Sb_{10}$ composition, which is within one standard deviation from the room-temperature one. The final crystallographic and atomic parameters for the crystal at 238 K are standardized through the program TIDY[21] and are summarized in Tables 2 and 3.

At 233 K, near the second transition temperature, the diffraction spots could be indexed to the above-mentioned monoclinic cell. Cooling to 228 K, below the second transition temperature, led to the formation of the *C*-centered supercell with $a = 32.637(5)$ Å, $b = 12.246(2)$ Å, $c = 10.876(1)$ Å, $\alpha = 90$, $\beta = 99.100(4)$, and $\gamma = 90°$, which was reported before.[3,15] As indicated by Nylen et al.[3] for 150 K, this cell has triclinic symmetry ($C\bar{1}$) but is metrically monoclinic. We could not perform a satisfactory structure solution and refinement of the 228 K data because of the small number of superstructure reflections observed. Further cooling to 203 K produced extra diffraction spots that could not be fitted to the cell observed at 228 K (Figure 6). Although some of the partial indices may have indicated tripling of the *c* parameter (e.g., see the two spots with the *hkl* values of −3 3 3.30 and −3 3 3.62 in Figure 6), the separation between them and the main diffraction spots was not regular (e.g., see the −3 3 4.25 reflection in Figure 6), which is a sign of an *incommensurably* modulated *c* parameter. In addition, there were diffraction spots that clearly expressed the incommensurate nature of the unit cell in the two other directions, *a* and *b*. Attempts were made to establish an approximate structure of this low-temperature (203 K) form using only reflections from the *C*-centered supercell by utilizing the structural model of Nylen et al.[3] and introducing twin laws. However, the refinement was not successful: the difference electron density map was very rough with a number of large electron density peaks closely spaced to the existing Zn atoms. Indeed, this was an expected outcome because the additional reflections were of significant intensity, which indicated a large structural modulation.

High-Temperature, Single-Crystal XRD. High-temperature XRD was done on a Bruker SMART Apex CCD diffractometer with Mo Kα radiation, equipped with a Nonius crystal heater.[22] To minimize oxygen and nitrogen contamination, no glue or cement was used for mounting the crystal, which was extracted from the polycrystalline sample. The crystal was put at the bottom of the 0.2 mm capillary and fixed in place by another thinner capillary (Hampton research #50 glass capillaries), and then the outer capillary was sealed off with argon inside.[23] Sixty frames were recorded at 293, 473, 573, 673, and 773 K to identify phases and determine unit cell parameters. The *a* and *c* parameters, as well as the *c*/*a* ratio, increase with temperature (Figure 7). Heating to 773 K, above the $\beta \rightarrow \gamma$ transition temperature of 767 K, produced a diffraction pattern similar to that of a crystal with many components. Attempts to derive unit cell symmetry and dimensions were unsuccessful. However, when the crystal was cooled to 753 K, 15 min after the temperature was raised to 773 K, the Bragg peaks could be indexed to multiple ZnSb components. Visual inspection of the capillary indicated that its inner walls were covered with a thin black deposit, which is mostly likely to be zinc lost by the crystal ($Zn_{13}Sb_{10} \rightarrow 10ZnSb + 3Zn$). Thus, these studies agree with X-ray powder diffraction results on the bulk polycrystalline sample, which showed decomposition of Zn_4Sb_3 at high temperatures (Figure 4).

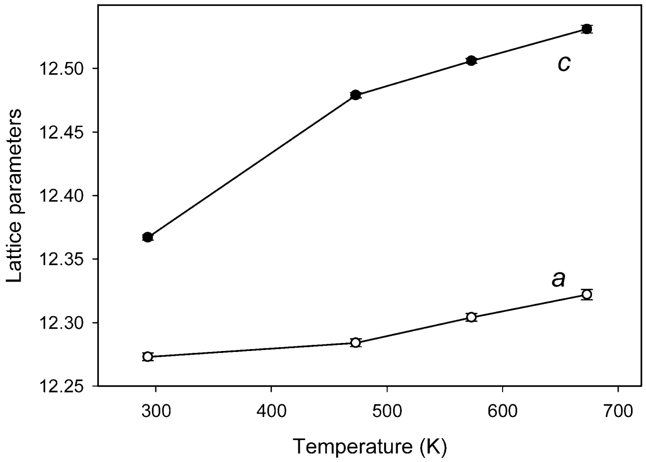

Figure 7. Lattice parameters of the β-phase as a function of temperature during heating (single-crystal data).

Electronic Structure Calculations. To understand the relationship between the structure, composition, and physical properties of $Zn_{13}Sb_{10}$, tight-binding linear-muffin-tin-orbital calculations using the atomic sphere approximation (TB-LMTO-ASA)[24] were carried out for the $Zn_{12}Sb_{10}$ motif of the room-temperature structures of $Zn_{13}Sb_{10}$. The main Zn sites were assumed to be fully occupied, and the interstitial Zn atoms were neglected. To satisfy the overlap criteria of the atomic spheres in the TB-LMTO-ASA method, empty spheres were included into the unit cell. For the $Zn_{12}Sb_{10}$ composition (74 electrons/formula), the Fermi level is located in the upper part of the valence band. Assuming the rigid band model, the valence band is filled at 76 electrons/formula, which corresponds to the $Zn_{13}Sb_{10}$ composition (see Figure 11).

Results and Discussion

A thorough structural study of the phase transitions in Zn_4Sb_3 below ambient temperature is complicated by the presence of disorder associated with certain Zn sites as well as the relatively narrow temperature range for existence of one of the phases. Characterization by diffraction as well as physical property measurements are critical to establish a sound picture of how these samples behave. However, as we have seen, flux-grown crystals and polycrystalline samples exhibit characteristics optimal for one characterization method and not for another. Our results indicate the existence of an intermediate phase between the low-temperature α-form and the ambient-temperature β-form in the temperature range of about 234−254 K.

Symmetry-Breaking Transitions and Landau Theory. The possibility of a phase transition being second-order in nature can be examined using Landau theory.[25,26] This theory gives symmetry constraints for symmetry-breaking transi-

---

[22] Tuinstra, F.; Storm, G. M. F. *J. Appl. Crystallogr.* **1978**, *11*, 257−259.

[23] Mozharivskyj, Y.; Pecharsky, A. O.; Pecharsky, V. K.; Miller, G. J. *J. Am. Chem. Soc.* **2005**, *127*, 317−324.

[24] Andersen, O. K.; Pawlowska, Z.; Jepsen, O. *Phys. Rev. B* **1986**, *34*, 5253−5269.

[25] Landau, L. D.; Lifshitz, E. M. *Statistical Physics (Course of Theoretical Physics)*, 2nd ed.; Pergamon Press, Ltd.: London−Paris, 1968; Vol. 5.

tions; that is, it answers the question whether a transition between the high- and low-symmetry structures can occur as a continuous (second-order) one. The theory can also provide a structural model for one of the phases during the continuous symmetry-breaking process.[27] Application of Landau theory to structural transitions involves several steps: (1) determination of a wavevector **k** corresponding to the distortion; (2) determination of irreducible representations of the **k** vector; (3) analysis of irreducible representations for absence of a third-order invariant in the expansion of the Gibbs free energy in the order parameter; (4) finding minima in the Gibbs free energy with respect to the basis functions of the relevant irreducible representations; (5) determination of space groups from the invariance of the Gibbs free energy under the symmetry operations; and (6) verification that a minimum in the Gibbs free energy as a function of the **k** vector is fixed by symmetry in the reciprocal space.

$R\bar{3}c \rightarrow C2/c$ Symmetry Reduction ($T = 254$ K). Because no superstructure is created during the phase transition at 254 K (the primitive cells of the rhombohedral and monoclinic lattices are similar), the wavevector of the distortion is $\mathbf{k} = 0$ and irreducible representations of **k** are isomorphous with those of the D_{3d} point group of the $R\bar{3}c$ space group. There are five irreducible representations breaking the symmetry: three one-dimensional and two two-dimensional. The one-dimensional representations yield space groups containing a threefold axis and are not of interest because they are not consistent with our observations. The two-dimensional irreducible representations, E_g and E_u, do not produce any third-order invariants in the expansion of the Gibbs free energy in the order parameter and, thus, can correspond to a continuous, symmetry-breaking transition within the Landau framework. Minimization of the Gibbs free energy with respect to the basis functions gives two identical solutions for the E_g and E_u representations. The resulting particle density, ρ, can be expressed as a sum of that of the symmetrical form, ρ°, and the two basis functions:

Solution 1 (E_g and E_u):

$$\rho = \rho^\circ \pm \frac{1}{\sqrt{2}}\eta(\varphi_1 + \varphi_2)$$

Solution 2 (E_g and E_u):

$$\rho = \rho^\circ + \frac{1}{\sqrt{2}}\eta(\pm\varphi_1 \mp \varphi_2)$$

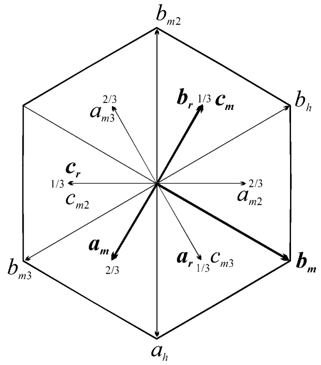

Figure 8. Relationships between the rhombohedral, hexagonal, and monoclinic unit cells. Three monoclinic unit cells, *m*, *m*2, and *m*3, are formed during the $R\bar{3}c \rightarrow C2/c$ symmetry breaking. The thick lines denote the unit cell vectors of the monoclinic cell chosen as a reference. The numbers 1/3 and 2/3 are the *z* coordinates (in the hexagonal cell) of the ends of the rhombohedral and monoclinic unit cell vectors.

Table 4. Matrix Representation of the Two-Dimensional Irreducible Representation E_g of the $R\bar{3}c$ Space Group at k = 0

g	E	C_{3z}	$C_{3z}{}^2$	C_{2y}	$C_{2(x+y)}$	C_{2x}
	$\begin{pmatrix}1 & 0\\0 & 1\end{pmatrix}$	$\begin{pmatrix}0 & -1\\1 & -1\end{pmatrix}$	$\begin{pmatrix}-1 & 1\\-1 & 0\end{pmatrix}$	$\begin{pmatrix}-1 & 0\\-1 & 1\end{pmatrix}$	$\begin{pmatrix}0 & 1\\1 & 0\end{pmatrix}$	$\begin{pmatrix}1 & -1\\0 & -1\end{pmatrix}$
g	I	$\bar{C}_{3z}$	$\bar{C}_{3z}{}^2$	σ_y	σ_{x+y}	σ_x
	$\begin{pmatrix}1 & 0\\0 & 1\end{pmatrix}$	$\begin{pmatrix}0 & -1\\1 & -1\end{pmatrix}$	$\begin{pmatrix}-1 & 1\\-1 & 0\end{pmatrix}$	$\begin{pmatrix}-1 & 0\\-1 & 1\end{pmatrix}$	$\begin{pmatrix}0 & 1\\1 & 0\end{pmatrix}$	$\begin{pmatrix}1 & -1\\0 & -1\end{pmatrix}$

The symmetry elements remaining upon symmetry breaking and, thus, the resulting space groups follow from the invariance of the particle densities under the operations of the $R\bar{3}c$ space group. Only for solution 1 of the E_g irreducible representation (Table 4) does the particle density remain identical under the $(C_{2(x+y)}|c_h/2)$, $(i|0)$, and $(\sigma_{(x+y)}|c_h/2)$ operations of the $R\bar{3}c$ space group (c_h is a translation along the c axis in the hexagonal setting, and $c_h = a_r + b_r + c_r$). The standard monoclinic setting (the C_2 axis parallel to b_m) can be achieved through the following transformations:

$$\begin{pmatrix}a_m\\b_m\\c_m\end{pmatrix} = \begin{pmatrix}1 & 0 & 1\\1 & 0 & -1\\0 & 1 & 0\end{pmatrix}\begin{pmatrix}a_r\\b_r\\c_r\end{pmatrix}$$

The monoclinic cell is *C*-centered as a result of the presence of the $^1/_2\ (a_m + b_m) = a_r$ translation. In the new cell, the $(C_{2(x+y)}|c_h/2)$ operation becomes $(C_{2y}|(a_m + b_m)/2)$, and $(\sigma_{(x+y)}|c_h/2)$ transforms into $(\sigma_y|(b_m + c_m)/2)$ under the *C*-centering translation. Combination of these two symmetry operations constitutes the $C2/c$ space group. Finally, an origin shift by $(a_m + b_m)/4$ puts all symmetry elements into a standard setting, with the inversion center at the origin. Presence of the inversion center locks the minimum of the Gibbs free energy at $\mathbf{k} = 0$, which excludes further structural modulation around $\mathbf{k} = 0$ and, thus, proves that the $R\bar{3}c \rightarrow C2/c$ symmetry reduction can be continuous (second-order) in nature. Equivalence of the three two-fold axes in the $R\bar{3}c$ space group implies three $R\bar{3}c \rightarrow C2/c$ distortion pathways (Figure 8) and, thus, the possibility of twinning. Twin laws for two components with respect to a component chosen as a “reference” are

$$\begin{pmatrix}1/2 & 1/2 & 1\\-1/2 & -1/2 & 1\\1/2 & -1/2 & 0\end{pmatrix}\quad \text{(twin component 2)},$$

$$\begin{pmatrix}1/2 & -1/2 & 1\\1/2 & -1/2 & -1\\1/2 & 1/2 & 0\end{pmatrix}\quad \text{(twin component 3)}$$

---

(26) Franzen, H. F. *Physical Chemistry of Solids*; World Scientific: Singapore, 1994.

(27) Mozharivskyj, Y.; Franzen, H. F. *Book of Abstracts*, Proceedings of the 219th ACS National Meeting, San Francisco, CA, March 26−30, 2000; American Chemical Society: Washington, DC, 2000; INOR-592.

Table 5. Matrix Representation of the Two-Dimensional Irreducible Representations of the $C2/c$ Space Group at $\mathbf{k} = {}^1/_4 c_m$

g	E	σ_y	i	C_{2y}
Γ'	$\begin{pmatrix}1 & 0\\0 & 1\end{pmatrix}$	$\frac{1}{\sqrt{2}}\begin{pmatrix}1 & -1\\1 & 1\end{pmatrix}$	$\begin{pmatrix}1 & 0\\0 & -1\end{pmatrix}$	$\frac{1}{\sqrt{2}}\begin{pmatrix}1 & 1\\1 & -1\end{pmatrix}$

g	E	σ_y	i	C_{2y}
Γ''	$\begin{pmatrix}1 & 0\\0 & 1\end{pmatrix}$	$\frac{1}{\sqrt{2}}\begin{pmatrix}-1 & 1\\-1 & -1\end{pmatrix}$	$\begin{pmatrix}1 & 0\\0 & -1\end{pmatrix}$	$\frac{1}{\sqrt{2}}\begin{pmatrix}-1 & -1\\-1 & 1\end{pmatrix}$

These twin laws were employed during the structural refinement at 238 K.

$C2/c \rightarrow C\bar{1}$ ($P\bar{1}$) and $C2/c \rightarrow C1$ ($P1$) Symmetry Reductions ($T = 234$ K). The **k** vector of the low-temperature distortion can be found from the fact that any lost translation (vectors $\mathbf{T}_i$) yields nonintegral values for $\mathbf{k}\cdot\mathbf{T}_i/2\pi$. At 228 K, quadrupling of the c_m lattice parameter is observed, and, thus, the wave vector is $\mathbf{k} = {}^1/_4 c_m$. The c_m quadrupling produces the *I*-centered, triclinic (metrically monoclinic) cell, which is then transformed into a *C*-centered cell. The transformation from the *C*-centered, small monoclinic lattice into the *C*-centered triclinic superlattice is represented by the following matrix:

$$\begin{pmatrix}a_t\\b_t\\c_t\end{pmatrix} = \begin{pmatrix}-1 & 0 & -4\\0 & 1 & 0\\1 & 0 & 0\end{pmatrix}\begin{pmatrix}a_m\\b_m\\c_m\end{pmatrix}$$

While the matrix representations of the irreducible representations (Table 5) for the $C2/c$ space group at $\mathbf{k} = {}^1/_4 c_m$ are not readily available, they can be derived from the loaded representations from ref 28 followed by application of the fundamental theorem on the basis functions of the irreducible representations of a nonsymmorphic space group.[29] Neither of the two-dimensional representations, Γ' and Γ'', produces third-order invariants in the expansion of the Gibbs free energy, and invariance of the fourth-order terms leads to the following expression for both Γ' and Γ'':

$$G = G^\circ + A\eta^2 + C\eta^4$$

where G° is the Gibbs free energy of the $C2/c$ phase, η is the order parameter, and A and C are coefficients. In these representations, the particle densities take the form $\rho = \rho^\circ + \eta(\gamma_1\varphi_1 + \gamma_2\varphi_2)$ where $\gamma_1^2 + \gamma_2^2 = 1$. The above expression imposes no restrictions on the relationship between the coefficients, γ_1 and γ_2, of the basis functions φ_1 and φ_2. In a general case, when γ_1 and γ_2 can take arbitrary values constrained only by normalization ($\gamma_1^2 + \gamma_2^2 = 1$), the particle density function remains invariant only under the identity operation. However, in two specific cases, when $\gamma_1 = \pm 1$ and $\gamma_2 = 0$ or $\gamma_1 = \gamma_2 = \pm 1/2$, the particle density remains invariant under the $(E|0)$ and $(i|0)$ operations. In the general case, the resulting space group is $C1$ ($P1$), while, in the specific cases, the resulting space groups are $C\bar{1}$ ($P\bar{1}$).

The minimum in the Gibbs free energy during the $C2/c \rightarrow C1$ symmetry reduction is not fixed by symmetry at $\mathbf{k} = {}^1/_4 c_m$, and, thus, this transition can follow an incommensurate pathway, because a small variation in **k** will produce a new minimum in G:

$$G(\mathbf{k} + \delta\mathbf{k}) = G(\mathbf{k}) + \alpha\delta\mathbf{k} + ...$$

Thus, this transition will be first-order in nature.

Development of reflections with fractional indices below the transition temperature during our experiments indicates that the low-temperature transition is likely to follow the $C2/c \rightarrow C1$ symmetry reduction accompanied by incommensurate modulation. Thus, this transition is first-order according to Landau theory. Some future experiments will be performed to establish the symmetry of this incommensurate structure and test our theoretical conclusions. On the other hand, the $C2/c \rightarrow C\bar{1}$ distortion observed by Nylen et al.[3] is confined to $\mathbf{k} = {}^1/_4 c_m$, because the minimum in G is fixed by the inversion center. Although all Landau conditions are met and this symmetry breaking can be continuous, there is also a possibility that the $C2/c \rightarrow C\bar{1}$ transition is first-order in nature.[30]

An unusual aspect of this low-temperature transition is the possibility of a structural distortion along two distinct routes: commensurate $C2/c \rightarrow C\bar{1}$ or incommensurate $C2/c \rightarrow C1$. The extension of the Gibbs free energy in the order parameter does not answer which distortion is thermodynamically preferred. However, from the Gibbs free energy/entropy relationship, it can be stated that the structure with higher entropy, that is, the $C\bar{1}$ one, is more stable than the $C1$ structure especially at higher temperatures, provided the enthalpy change is equal along the two distortion pathways. If, however, there is a larger enthalpy gain (e.g., in electronic energy) during the $C2/c \rightarrow C1$ symmetry reduction, the distortion will follow this path. The preference for $C\bar{1}$ or $C1$ symmetry may be influenced by the Zn/Sb ratio or presence of impurities. It is also likely that because of slight crystal inhomogeneities, different domains of the crystal may exhibit different symmetries.

Structural Analysis. The idealized $Zn_{12}Sb_{10}$ (or Zn_6Sb_5) atomic motif of the β-phase can be built from Sb atoms with Zn in tetrahedral voids.[15] Although that structural approach accounts for the 6:5 Zn/Sb ratio, it does not provide a rationale for either the $Zn_{13}Sb_{10}$ composition or the interatomic interactions and is also inconvenient for analyzing ordering of Zn atoms during the symmetry breaking. Recently, Häussermann et al. showed that interconnected Zn_2-$Sb(1)_2$ diamond units with multicenter bonding are essential in forming the idealized $Zn_{12}Sb_{10}$ framework.[33] These diamond units also account for the observed $Zn_{13}Sb_{10}$ composition as the $Zn_{12}Sb_{10}$ framework requires two more

---

(28) Kovalev, O. V. *Irreducible representations of the space groups*; Gordon and Breach, Science Publishers: New York, 1965.

(29) Cornwell, J. F. *Group Theory and Electronic Energy Bands in Solids*; North-Holland: Amsterdam, The Netherlands, 1969.

(30) Franzen, H. F. *Physical Chemistry of Inorganic Crystalline Solids*; Springer-Verlag: New York, 1986.

(31) Miller, G. J. In *Chemistry, Structure, and Bonding of Zintl Phases and Ions*; Kauzlarich, S. M., Ed.; VCH Publishers: New York, 1996; pp 1−59.

(32) Adolphson, D. G.; Corbett, J. D.; Merryman, D. J. *J. Am. Chem. Soc.* **1976**, *98*, 7234−7239.

(33) Mikhaylushkin, A. S.; Nylen, J.; Haeussermann, U. *Chem.*−*Eur. J.* **2005**, *11*, 4912−4920.

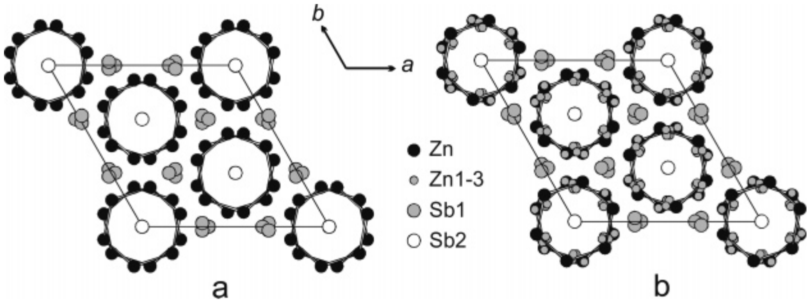

Figure 9. (a) Idealized $Zn_{12}Sb_{10}$ framework and (b) the refined structure of the room-temperature $Zn_{13}Sb_{10}$, as seen down the *c* axis.

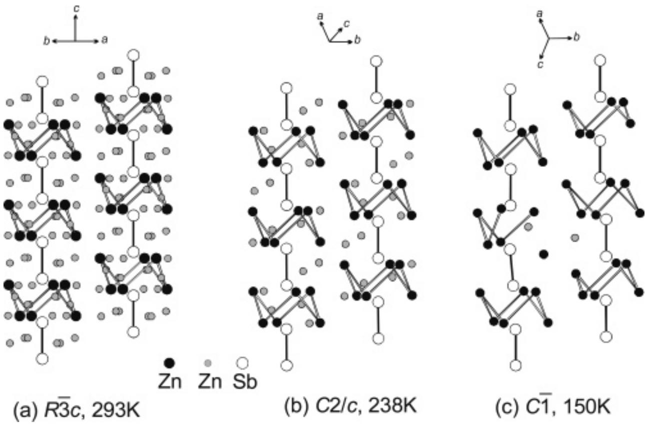

(a) $R\bar{3}c$, 293K (b) $C2/c$, 238K (c) $C\bar{1}$, 150K

Figure 10. Structures of the $Zn_{13}Sb_{10}$ polymorphs at (a) room temperature, (b) at 238 K, after the first symmetry breaking, and (c) at 150 K, after the second symmetry breaking.

electrons (from an additional Zn atom) to satisfy all bonding interactions. In Häussermann's approach, the additional Zn atoms of the room-temperature β-form were treated as simple electron donors to the $Zn_{12}Sb_{10}$ framework. To visualize major structural changes associated with the two phase transitions, we believe that a different structural representation, depicted in Figures 9 and 10 and similar to the one used by Nylen et al.,[3] is more beneficial. An idealized $Zn_{12}Sb_{10}$ framework of the rhombohedral $Zn_{13}Sb_{10}$ β-phase consists of the Zn channels centered by Sb2 atoms and with Sb1 atoms located between the channels (Figure 9a). As seen from the side (Figure 10a), the Zn channels are formed from six-membered crownlike rings that stack along the *c* axis and sandwich the Sb2−Sb2 dimers. In the room-temperature β-phase, additional Zn atoms (sites 1−3) are located along the channel walls (Figure 9b), and they can be found within and between the six-membered rings (Figure 10a). Some of the distances between the "main" and interstitial Zn atoms are quite short ($d_{\min} = 1.09$ Å), but because XRD yields the average crystal structure, the Zn atoms are not all necessarily present in the same unit cell. The Zn−Sb bonds are reasonable for both the main ($d_{\min} = 2.69$ Å) and additional ($d_{\min} = 2.55$ Å) Zn sites. The nearest neighbor interactions and possible ordering schemes are extensively discussed in ref 2.

The $R\bar{3}c \rightarrow C2/c$ transition leads to significant ordering of the interstitial Zn atoms, as reflected by a smaller number (Figure 10b) and correspondingly higher occupancy of the interstitial Zn sites (Table 3). This ordering can be visualized as a collapse of three interstitial Zn sites into one during the transition. Surprisingly, total occupancy of the resulting Zn sites surpasses the occupancy of the original Zn sites in the $R\bar{3}c$ structure. Similar, although somewhat less pronounced, is the increase in the total occupancy of the main Zn sites in the $C2/c$ structure. At present, there is no solid understanding of what causes this phenomenon. Most of the interatomic distances in the distorted $C2/c$ structure closely resemble those in the $R\bar{3}c$ structure. The largest change is observed for the shortest distance between the main and the interstitial Zn atoms: it increases from $d_{\min} = 1.09$ Å to $d_{\min} = 1.20$ Å.

The commensurate $C\bar{1}$ structure of the low-temperature α-polymorph (Figure 10c) is based on the data by Nylen et al.[3] Here, the interstitial Zn atoms are located on two fully occupied sites, and the main Zn sites are also fully occupied. This yields a stoichiometric $Zn_{13}Sb_{10}$ formula. Ordering associated with the $C2/c \rightarrow C\bar{1}$ symmetry reduction appears to be quite different from that of the $R\bar{3}c \rightarrow C2/c$ transition. During the $C2/c \rightarrow C\bar{1}$ transition the interstitial Zn atoms go into the main Zn sites until these sites are completely filled, and then the remaining Zn atoms order on two individual sites, whereas the interstitial Zn atoms seem to order on fewer interstitial sites during the $R\bar{3}c \rightarrow C2/c$ transition. This distinct ordering behavior has its structural consequences. Because in the $R\bar{3}c$ and $C2/c$ phases both the main and the interstitial Zn sites within the crownlike rings are deficient, they can occupy geometrically the same space but in different unit cells. However, in the $C\bar{1}$ polymorph all sites are fully occupied and the presence of interstitial Zn atoms within the crownlike rings introduces local structural perturbations, which distorts these rings (Figure 10c).

Composition, Electronic Structure, and Electrical Conductivity. The microprobe analysis yielded the $Zn_{56.5(1)}Sb_{43.2(2)}Bi_{0.35(2)}$ (or $Zn_{13.00(2)}Sb_{9.94(5)}Bi_{0.080(5)}$) composition for the flux-grown single crystals of the room-temperature β-phase. Assuming presence of Bi just on the Sb site, the formula of a Bi-free crystal can be written as $Zn_{13.00(2)}Sb_{10.02(6)}$, which is within one standard deviation from the stoichiometric $Zn_{13}Sb_{10}$ composition. The $Zn_{13}Sb_{10}$ composition was obtained by Nylen et al. from the low-temperature single-crystal refinement of the ordered α-structure.[3] Inaccuracies in the compositions $Zn_{11.8(2)}Sb_{10}$ and $Zn_{12.0(2)}Sb_{10}$ refined from our X-ray single-crystal data at 293 and 238 K are likely to stem from both extrinsic factors related to the XRD (absorption, extinction, etc.) and intrinsic factors associated with highly disordered structures (interstitial Zn atoms can be present on more than three sites with smaller occupancies).

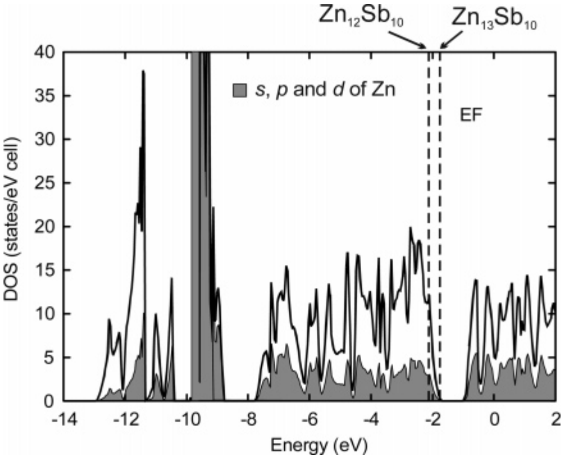

Figure 11. Total and partial DOS calculated assuming an idealized $Zn_{12}Sb_{10}$ framework of β-$Zn_{13}Sb_{10}$. Dashed lines show positions of the Fermi level for the two compositions.

When Zn−Zn interactions in $Zn_{13}Sb_{10}$ are neglected, the Zintl−Klemm formalism for valence compounds[31] provides an accurate electron count. The Sb1 atoms in the $R\bar{3}c$ structure (Sb1-2 atoms in the $C2/c$ structure) have no Sb neighbors and can be treated as Sb^{3-}. The Sb2 atoms in the $R\bar{3}c$ structure (Sb3 atoms in the $C2/c$ structure) form dimers with $d_{Sb-Sb} = 2.82$ Å, which is characteristic of a Sb−Sb single bond,[32] which is isoelectronic with a halogen dimer and carries a formal charge of −2. Six $Sb1^{3-}$ and four $Sb2^{2-}$ in $Zn_{13}Sb_{10}$ require 26 electrons that are provided by 13 Zn atoms. However, the presence of Zn−Zn bonds of 2.78 Å makes this phase electron deficient and, thus, metallic from the Zintl−Klemm closed shell approach. Recently, Haussermann et al.[33] showed that this electron deficiency is overcome by the formation of interconnected structural units with distinctive bonding: rhomboid rings made from two Zn and two Sb1 atoms. The four-center bonding within these rings is optimized with four electrons, that is, with less electrons which otherwise would be required if the constituent atoms of the rings were participating in two-center two-electron bonds.

The fact that $Zn_{13}Sb_{10}$ is indeed electron precise is recognized in the band structure (Figure 11). The band gap of ~0.8 eV separates the valence and conduction bands. Assuming a rigid band model, the valence band is filled at 76 electrons/formula. The structural features, especially bonding characteristics of two different Sb atoms, are also recognizable in the density of states (DOS). The lower part (−13 to −10.5 eV) of the DOS contains five peaks. The two lower and two upper peaks are indicative of dimer formation within a linear atomic chain, and they are derived from the Sb2 5s states with some Zn contribution. The larger, middle peak at −11.5 eV showing localized character typical of monomers comes from Sb1 5s orbitals. Large DOS between −10 and −9 eV represent the localized Zn d orbitals that do not contribute much to either Zn−Sb or Zn−Zn bonding. The valence band (−7.7 to −1.7 eV) consists mostly of Sb 5p and Zn 4s orbitals and represents bonding states of the Zn−Sb, Zn−Zn, and Sb2−Sb2 interactions.

The ideal $Zn_{13}Sb_{10}$ composition implies full occupancy of the valence band and, thus, intrinsic semiconducting behavior. However, the resistance measurements for both polycrystalline and single-crystal samples (Figure 1) show metallic-type conductivity. This metallic-type behavior and a relatively large value of resistivity of the flux-grown crystal are characteristic of heavily doped semiconductors. In this material, this can occur from either Zn deficiencies (*p*-type doping) or excess of Sb atoms (*n*-type doping). From structural considerations, Zn deficiencies are more likely to be present in the structure and, thus, to dictate the nature of the electrical conductivity. This conclusion agrees with the results by Caillat et al.,[5] who established that the majority of the carriers in Zn_4Sb_3 are holes.

Conclusions

XRD studies and resistance measurements on Zn_4Sb_3 indicated the presence of two low-temperature phase transitions, each being accompanied by a symmetry reduction. According to Landau theory, the first $R\bar{3}c \rightarrow C2/c$ symmetry breaking may be second-order in nature. From theoretical considerations, the subsequent symmetry breaking can proceed along two routes: commensurate $C2/c \rightarrow C\bar{1}$ or incommensurate $C2/c \rightarrow C1$. Our experimental results indicate a first-order nature and incommensurate pathway for this transition, both of which are consistent with the $C2/c \rightarrow C1$ symmetry reduction.

Quantitative microprobe analysis yielded only slight Bi doping of flux-grown crystals and proved that the composition of the Bi-free phase is better represented with the $Zn_{13}Sb_{10}$ formula. The $Zn_{13}Sb_{10}$ composition implies full occupancy of the valence band and semiconducting behavior of the resistance. However, the resistance measurements point to the presence of some empty states in the valence band. XRD studies and Seebeck coefficient measurements revealed instability of the $Zn_{13}Sb_{10}$ phase with respect to Zn losses at high temperatures in a vacuum.

Acknowledgment. The authors are grateful to H. B. Rhee and P. C. Canfield for their invaluable support during the single-crystal preparation. This manuscript has been authored by Iowa State University of Science and Technology under Contract No. W-7405-ENG-82 with the U.S. Department of Energy. The research was supported by the Office of Basic Energy Sciences, Materials Science Division, U.S. DOE.

Supporting Information Available: Crystallographic information (CIF). This material is available free of charge via the Internet at http://pubs.acs.org.

CM0515505